






Introducing Inharmonic Radar: Tag Detection in the Automotive Bands of Present and Future at 76–81/134–141 GHz via Fractional Multiplication

TOBIAS T. BRAUN ¹ (Graduate Student Member, IEEE), JAN SCHÖPFEL ¹ (Member, IEEE),
CHRISTIAN BREDENDIEK ² (Member, IEEE), JUAN JOSE FORERO B. ¹,
AND NILS POHL ^{1,2} (Senior Member, IEEE)

(Regular Paper)

¹Institute of Integrated Systems, Ruhr University Bochum, 44801 Bochum, Germany

²Fraunhofer Institute for High Frequency Physics and Radar Techniques, 53343 Wachtberg, Germany

CORRESPONDING AUTHOR: Tobias T. Braun (e-mail: tobias.t.braun@rub.de).

This work was supported in part by the German Federal Ministry of Education and Research (BMBF) in part in the course of the Research Project VERANO under Grant 16ME0793 and in part by the Project SafeMe under Grant 16ME0886.

ABSTRACT Harmonic radar systems are highly effective at distinguishing specific targets from surrounding clutter. Therefore, the reception of a tag response, conventionally at the second harmonic, is utilized. Thus, necessitating two bands with that specific spacing allocated to the same application. Among others, this is not the case for automotive, where tag-based detection of vulnerable road users in city traffic has shown promising results. Therefore, we introduce the novel nonlinear radar category of inharmonic radar. It is based on fractional multiplication, to enable a wider range of possible factors. Specifically, the automotive band at 76–81 GHz is connected with the 134–141 GHz frequency range by a factor of 1.75. The realized system achieves a clutter rejection of 60 dB, which is investigated in detail regarding influences of the inharmonic approach. Detection of the corresponding tag is successfully achieved up to a distance of 28 m with compliance for automotive radar, while no significant spectral purity degradation is caused by the unique frequency conversion.

INDEX TERMS Automotive, clutter suppression, *D*-band, frequency-modulated continuous wave (FMCW), harmonic, inharmonic, millimeter-wave (mm-wave), radar, SiGe, tag, vulnerable road users, *W*-band.

I. INTRODUCTION

Over half a century ago, in 1973, the concept of harmonic radar was invented [1]. The intended application of automotive radar itself was still in its infancy after just having been proposed in the 1960s with the visionary idea to eventually automate traffic [2]. It was long before automotive radar systems at 77 GHz tapped into the mass market [3] and interference mitigation became an increasing concern [4]. Nevertheless, the harmonic approach aimed to reduce rear-end collisions by distinguishing the reflections of the preceding vehicle from crosstalk with adjacent lanes. In other words, increasing the Signal-to-clutter ratio (SCR). Therefore, the front driving rear

end was equipped with a so-called tag, consisting of a receive antenna, frequency doubler, and transmit antenna. Down-converting with the doubled transmit signal at the reader in the car driving behind clearly distinguished between tagged and non-tagged objects.

Decades passed without further adoption of the measurement principle until the turn of the millennium, when it drew considerable interest for a completely different application: insect tracking [5], [6], [7]. Harmonic radar increases the SCR significantly when detecting a tiny insect with a low radar cross-section (RCS) near ground level. With the extensive implementation of radio-frequency identification (RFID), the

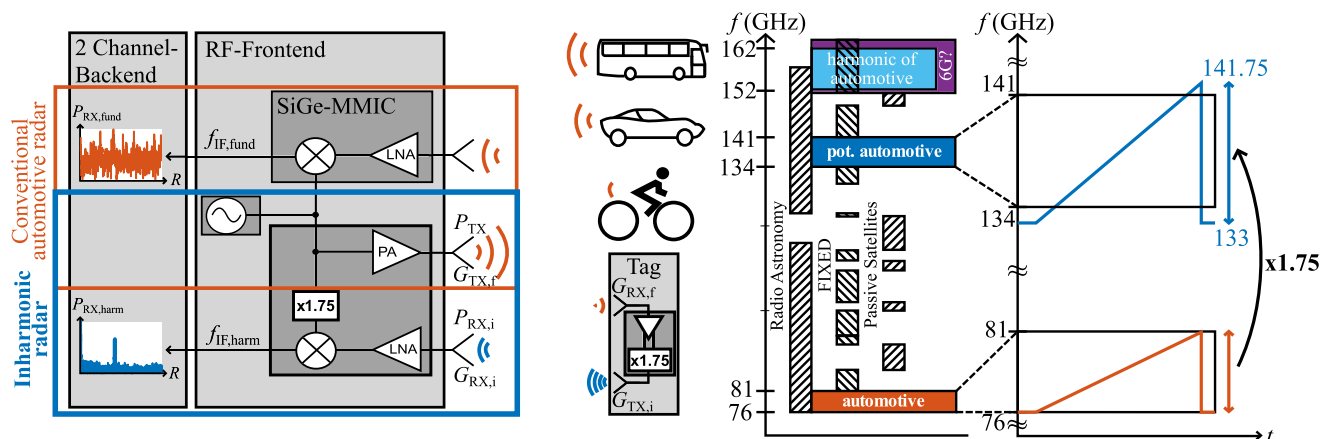


FIGURE 1. Block diagram of the proposed radar system. The tag amplifies the signal before frequency multiplication. This allows for its detection in a clutter-free receive channel. Utilizing the potential future automotive band from 134–141 GHz is proposed for spectral compliance. This new band can be fully covered from the current 76–81 GHz band by a factor of 1.75, with a 76.57–80.57 GHz chirp.

concept is currently reconsidered for different applications where SCR is a concern and has garnered more interest than ever. Applications include avalanche [8] and maritime search and rescue [9], joint angle estimation [10], 5G cyber-physical systems [11], and industrial localization [12].

All the systems above are based on frequency doubling, while some work utilizing the third harmonic exists [13], [14], [15]. Doubling comes with the advantage of being easily realizable via several approaches, such as Schottky diodes [16] or nonlinear transmission lines [17]. Even at mm-wave frequencies, where active tags are required, different frequency doubler topologies are utilizable [18]. However, it introduces a different major challenge for harmonic radar: spectral compliance. Very few bands offer a fundamental and harmonic frequency for the same application. It is mainly limited to Industrial, Scientific, and Medical (ISM) [17], including the bands at 61/122 GHz targeted in [19]. Applying the benefits of clutter-free tag detection to other applications, therefore, requires an adaptation of the harmonic radar concept to enable spectral compliance.

This adaptation is the topic of this article. As the targeted application, we chose automotive, the original from the invention of harmonic radar. Where we ourselves have proposed a corresponding system to detect vulnerable road users, who account for an increasing proportion of traffic fatalities, more reliably [20], [21], [22]. While the system results were very promising, the harmonic frequencies from 152–162 GHz are not licensed for automotive. They instead are part of a larger frequency band ranging from 151.5–164 GHz currently considered for 6G [23], [24]. Thus preventing the usual frequency doubling and qualifying it as a prime example for developing a revised approach. Therefore, we presented an active tag integrated circuit based on a novel 1.75 times frequency multiplier in [25]. Multiplication of 76–81 GHz by that factor results in 133–141.75 GHz, thereby connecting the current automotive radar frequencies with a potential new band [26]. In other words, a transmit chirp of 76.57–80.57 GHz fully covers the frequencies from 134–141 GHz when multiplied by

1.75. This frequency range was already targeted in research with the design of corresponding transceivers [27], [28], and its use in exterior vehicular radar was recently supported by a decision of the ECC [29]. It also introduces the opportunity for clutter-free tag-based detection with spectral compliance.

Realizing this vision and therefore proving the validity of fractional multiplication in tag-based radar is the topic of this article. Therefore, a radar system allowing for the clutter-free detection of the previously presented tag chip is implemented. Its functional block diagram and an overview of the frequency regulation are presented in Fig. 1. Due to the fractional frequency multiplication, we propose to call the adapted approach inharmonic radar, in harmony with music theory [30]. Therein, inharmonicity describes the degree to which the overtones' frequencies depart from the fundamental frequency's harmonics. Thus resulting in fractional frequency multiples. The realized system is intended to act as an example of enabling high SCR tag detection with spectral compliance in arbitrary applications based on such a frequency conversion. Thus solving a major challenge caused by harmonic radar utilizing only integer multiples and adding a new category to nonlinear radar systems [31].

Therefore, Section II discusses the inharmonic frequency generation with the necessary integrated circuits presented in Section III. The inharmonic radar system is described in Section IV. System measurements and comparisons to harmonic radar are shown and discussed in Section V, with a comparison to the state of the art in Section VI and conclusion in Section VII.

II. INHARMONIC FREQUENCY GENERATION

To successfully implement the inharmonic radar system shown in Fig. 1, a 1.75 times fractional frequency multiplier is needed inside the tag and inharmonic receiver. In contrast to frequency doubling or generating other harmonics via multiplication, way less work on generation of inharmonics exists.

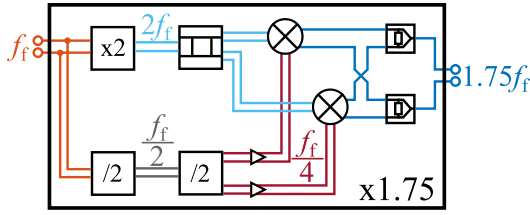


FIGURE 2. Block diagram of the proposed frequency multiplier. To generate $1.75f_f$, a quarter of the input frequency is subtracted from its doubled signal with an SSB-mixer [25].

A. REALIZATION OF THE DESIRED FACTOR

Whole synthesizers can generate not just integer, but also fractional multiples of a given reference frequency. While fractional phase-locked loops (PLLs) are able to achieve a resolution depending on the bit depth of the delta-sigma modulator [32], they bring significant complexity and their multiplication factors are generally too high. In [33] such a PLL is combined with multiple injection-locked multipliers (ILM) and dividers to cover a range of frequency bands in what is called a subharmonic injection-locked (SHIL) synthesizer.

Along the same line, a 1.5 times frequency multiplication by itself is implemented in [34] by injection locking a tripler to the output of a $/2$ -divider. However, with the desired multiplication factor of 1.75 equaling $7/4$, a $/4$ -divider would have to be combined with a 7 times multiplier to utilize the same approach. Even for the latter by itself, realizations are rare, with high spectral purity being challenging [35]. Odd-harmonic frequency multipliers, such as triplers, utilize inherent nonlinearities of the transistor as well as distortions based on operation in saturation [36]. Higher factors are favorably separated into multiple stages [37]. However, seven being a prime number prevents this approach, making it especially challenging.

Instead, utilizing mixers allows for flexible frequency multiplication as was shown for odd-harmonics [38], as well as inharmonics [39]. Along those lines, we proposed the utilization of a single-sideband (SSB) mixer to combine the doubled and quartered frequency to achieve the desired factor in [25]. This concept is shown as a block diagram in Fig. 2. Adding the outputs of the two individual Gilbert-cell mixers, as

$$\begin{aligned} s_{\text{out}}(t) &= \cos\left(2\pi\frac{f_f}{4}t\right) \cdot \sin(2\pi 2f_f t) \\ &\quad - \sin\left(2\pi\frac{f_f}{4}t\right) \cdot \cos(2\pi 2f_f t) \\ &= \sin(2\pi 1.75f_f t), \end{aligned} \quad (1)$$

exclusively results in the desired multiplication of the fundamental frequency f_f . The required I/Q signals for the doubled frequency are generated by a scaled version of the integrated hybrid coupler presented in [40]. For the quartered frequency, the divider provides the phase shifted signals intrinsically at the output of the two latches [41].

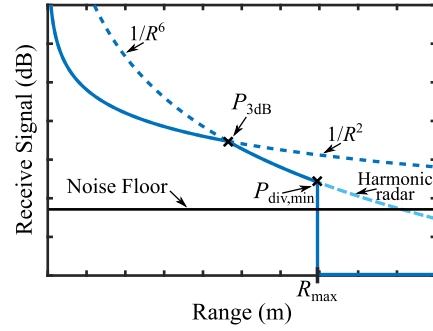


FIGURE 3. Proportionalities of the tag depending on the range. The longer the amplifier chain saturates the tag, it stays in the beneficial $1/R^2$ proportionality.

B. POWER TRANSFER FUNCTION

The power transfer function of this multiplier, and therefore the tag, dictates its dependency of the range R . In [19] and [21] this is investigated for active tags based on a Gilbert-cell doubler. It was shown that the range dependency deviates from the $1/R^4$ proportionality of conventional radar described by the Friis-equation given as

$$P_{\text{RX}} = \frac{P_{\text{TX}} \cdot G_{\text{TX}} \cdot G_{\text{RX}} \cdot \lambda^2 \cdot \sigma}{(4\pi)^3 \cdot R^4}, \quad (2)$$

with the system's output power P_{TX} , transmit and receive antenna gain, G_{TX} and G_{RX} , respectively, the signal's wavelength λ and the target's RCS σ . This is due to the nonlinear power transfer function of the frequency doubler. The introduction of the additional components inside the multiplier, especially the frequency divider with its input sensitivity, results in a new region in the necessary case distinction.

Subsequently, the multiplier's output power P_{out} in dependency of the input power P_{in} is separated into three regions. Firstly, for high input powers at low ranges, the amplifier chain and doubler saturate, achieving their maximum output power. As long as this is the case, the multiplier in total achieves its saturated output power P_{sat} . Secondly, for a P_{in} too low to achieve saturation, the doubler's output power decreases quadratically, weighted by its conversion gain. The characteristic input power $P_{3\text{dB}}$ is defined where $P_{\text{out,doub}} = P_{\text{sat,doub}} - 3\text{dB}$. Depending on the sensitivity of the divider, it, however, still delivers its constant output power. The quadratic dependency of the doubler is therefore passed through the mixer-cells with their conversion gain to the multipliers output. Third and finally, for even lower input powers, the doubler will remain in its quadratic dependency, but the divider will stop working altogether once P_{in} falls below its minimum required input power $P_{\text{div,min}}$. Therefore, no power will be sent out at the desired frequency any longer.

Thus, the multiplier's P_{out} in dependency of P_{in} is described by:

$$P_{\text{out}} \propto \begin{cases} P_{\text{sat}}, & P_{\text{in}} \geq P_{3\text{dB}} \\ P_{\text{in}}^2, & P_{3\text{dB}} \geq P_{\text{in}} \geq P_{\text{div,min}} \\ 0, & P_{\text{div,min}} \geq P_{\text{in}}. \end{cases} \quad (3)$$

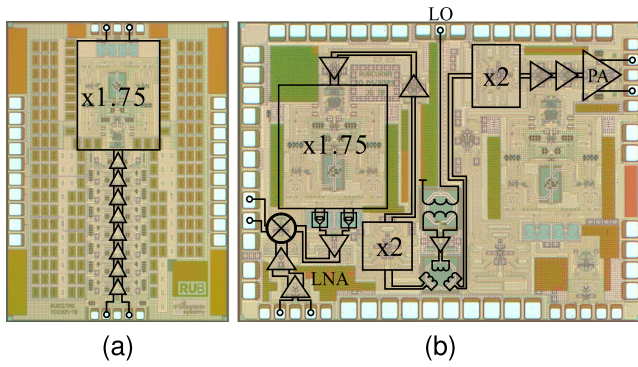


FIGURE 4. Photographs of (a) the tag MMIC presented in [25] and (b) the newly presented inharmonic transceiver MMIC. It encompasses one TX at the fundamental and two RX at the inharmonic.

Inside the inharmonic radar system, this will lead to a range dependency of the power received at the reader P_{RX} given by

$$P_{RX} \propto \begin{cases} 1/R^2, & P_{in} \geq P_3 \text{ dB} \\ 1/R^6, & P_3 \text{ dB} \geq P_{in} \geq P_{div,min} \\ 0, & P_{div,min} \geq P_{in}. \end{cases} \quad (4)$$

Those proportionalities are illustrated in Fig. 3 in comparison to harmonic radar, where the third region caused by the divider does not exist. They are expected to occur in the system measurements when moving the tag away from the reader in Section V-F.

III. MONOLITHIC MICROWAVE INTEGRATED CIRCUITS (MMIC)

Enabling those system measurements requires two MMICs: the tag and a transceiver which allows for the detection of said tag. Both MMICs are manufactured in Infineon's 130 nm B11HFC SiGe:C technology with an $f_T = 250$ GHz and $f_{max} = 370$ GHz.

A. TAG MMIC

As mentioned, the former has been presented in [25] and is shown in Fig. 4(a). In front of the 1.75 times frequency multiplier, it also encompasses the amplifier chain consisting of eight amplifiers, as presented in [21]. Their importance is further increased due to the revised power transfer function presented in the previous chapter and (3). In harmonic radar, the doubler successfully implements the frequency conversion even for very low input powers, albeit with decreasing conversion gain. In this inharmonic radar, the multiplication will stop working for too low input powers due to the divider's input sensitivity. The amplifier chain will stop that from happening for as high of a range between tag and reader as possible, by providing an adequate input power if its gain is sufficient. Thereby, it enables the tag to successfully implement the necessary frequency conversion upwards of an input power of -53 dBm at $f_{out} = 137.5$ GHz with an expected differential $P_{sat} = -9$ dBm. In total, the tag chip's dimensions are $1448 \times 1964 \mu\text{m}^2$ with an active area of $500 \times 1790 \mu\text{m}^2$. It consumes a current of 120 mA from a 3.3 V power supply.

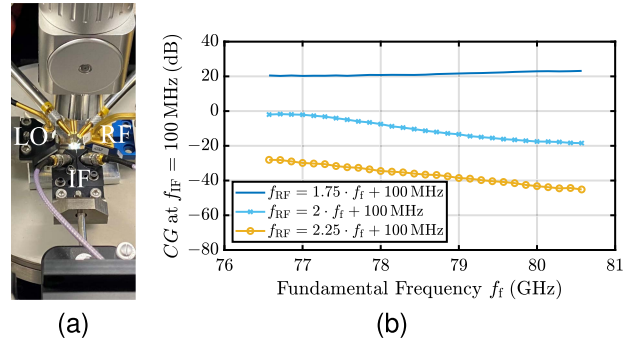


FIGURE 5. Measurement setup in (a) and measured conversion gain in dependency of the fundamental frequency f_f for a fixed $f_{IF} = 100$ MHz in (b). For the desired inharmonic a conversion gain upwards of 20 dB is achieved. Expected sidebands, are in comparison, suppressed by up to 42 dB and 68 dB, respectively.

B. INHARMONIC TRANSCIVER

Detecting the vulnerable road users equipped with the inharmonic frequency tag, requires the introduction of a corresponding transceiver MMIC, which is shown in Fig. 4(b). It offers two of the necessary inharmonic RX channels and one transmit channel for the fundamental automotive band. The MMIC is designed to work with the same LO-signal provided by the external voltage-controlled oscillator (VCO) presented in [21]. Therefore, it encompasses an LO input stage, which handles the single-ended to differential conversion and offers significant gain [42]. This allows for the potential utilization of multiple transceivers with one VCO output. Thus enabling multiple-input multiple-output (MIMO) systems based on time-division multiplexing (TDM). Since the VCO works sub-harmonically at $f_f/2$, each channel includes a separate frequency doubler, increasing the isolation between the channels.

Additionally, the TX channel consists of two buffers, as well as a power amplifier. The Class A cascode amplifier generates an output power of 15 dBm when measured on-chip. Additionally, it achieves a measured gain of 15 dB with a power added efficiency (PAE) of 12.5% [42]. The current consumption for the transmit channel adds up to 127 mA from a power supply of 3.3 V.

Newly required for the presented application is an RX for the inharmonic frequencies. Both included channels consist of a two-stage LNA, down-conversion mixer, and the same 1.75 times frequency multiplier utilized on the tag MMIC, respectively. Therefore, the divider's phase uncertainty should be considered, if the above mentioned MIMO systems are implemented [43]. The used channel consumes a current of 140 mA from a 3.3 V power supply. In simulations, the two-stage LNA, which is a scaled version of the schematic presented in [42], achieves a maximum gain of 14.5 dB with a minimum simulated noise figure of 9.3 dB in the 134–141 GHz frequency range. The subsequent down-conversion mixer utilized as a Gilbert cell achieves a simulated conversion gain CG of 4.5 dB. Altogether, this results in a simulated conversion gain of 19 dB.

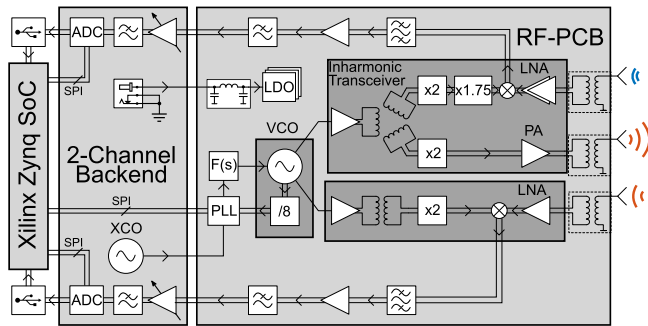


FIGURE 6. Block diagram of the realized reader. To combine the capabilities of conventional radar measurements with tag detection, it has one TX at the automotive band with one RX at the fundamental and inharmonic frequency band, respectively.

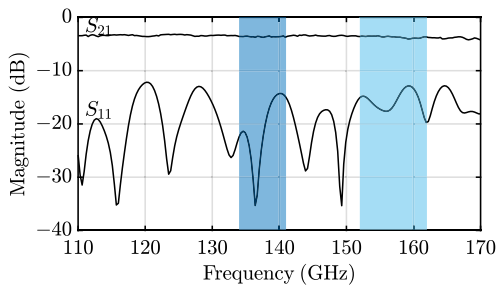


FIGURE 7. Measured S -parameters of the D-band waveguide transition of the reader presented in [21]. Due to it covering the whole WR6.5-band, it is also suitable for receiving the inharmonic frequencies.

To determine the receiver's gain in measurements, the inharmonic transceiver by itself is characterized on a probe-station, as depicted in Fig. 5(a). The corresponding LO-Signal at $f_f/2$ is provided by a PSG of Keysight Technologies and, as described, doubled to f_f inside the transceiver, before reaching the 1.75 times frequency multiplier. Its output signal is applied to the LO port of the switching quad of the Gilbert-cell acting as the down-conversion mixer. The RF-Signal is generated with a PNA-X, also by Keysight Technologies, in conjunction with a WR6.5-VNAX by Virginia Diodes. For a constant intermediate frequency $f_{IF} = 100$ MHz, a conversion gain of 20–23 dB is measured for the desired RF-frequency range of 134–141 GHz, as illustrated in Fig. 5(b).

Additionally, as the 1.75 times frequency multiplier will not generate the desired $1.75 \cdot f_f$ exclusively, the conversion gain of the strongest expected sidebands is also investigated and shown in Fig. 5(b). This should provide an insight into the expected filtering of the receiver should those sidebands also be reflected by the tag, or from other parasitic paths inside the system. Visualizing these components cohesively is the reason for plotting the fundamental frequency on the x-axis in this and other figures. While the sideband at $2 \cdot f_f$ could also be generated with the WR6.5-VNAX the subsequent WR5.1-VNAX by Virginia Diodes is used for the measurement of $f_{RF} = 2.25 \cdot f_f$. The corresponding results in principle show the capability of the RX to also receive the undesired sidebands. However, the attenuation of $2 \cdot f_f$ is in the range of

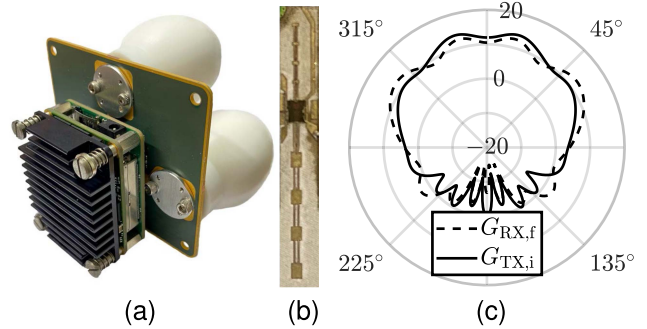


FIGURE 8. Photograph of the realized reader in (a), the tag portion of its respective PCB in (b), and the simulated gain of the tag's fundamental RX and inharmonic TX antenna, respectively, in (c).

22–42 dB and of $2.25 \cdot f_f$ within 49–68 dB. The sufficiency of that filtering will be further investigated in Section V.

IV. INHARMONIC RADAR SYSTEM

With those presented MMICs, the inharmonic radar system with spectral compliance for automotive applications can be realized. It consists of the reader and tag PCB.

A. READER

A detailed block diagram of the reader is shown in Fig. 6. In addition to the inharmonic transceiver presented in the previous section, it utilizes two further MMICs. Namely, the fundamental transceiver and VCO, as presented in [21]. The former enables simultaneous conventional radar measurements by receiving the reflections at the fundamental. This is considered important, as the non-tagged objects in traffic cannot just be considered clutter. Their detection and avoidance is also essential. Both the inharmonic and fundamental transceiver require an LO-signal subharmonic to the automotive band, which is provided by the VCO.

To cope with the high frequencies of the MMIC, the reader PCB is realized on Rogers RO3003 substrate, which is standard for automotive applications. It has a thickness of $127 \mu\text{m}$, a dielectric constant of $\epsilon_r = 3$ and a dissipation factor $\tan \delta = 0.001$ at 10 GHz. The top layer is used for routing and has a copper thickness of $35 \mu\text{m}$, while the bottom layer is 1 mm thick. This provides thermal capacity for the MMICs and allows for milling of stepped impedance waveguide transitions. As presented in [21] and shown in Fig. 7, the designed D-band transition covers the whole frequency range of the WR6.5 waveguide. It is therefore just as suitable for receiving the inharmonic frequencies, as it was for the harmonics. Advantageously, the inharmonic transceiver was designed to be pin or rather pad compatible to the harmonic transceiver of [21]. Thus, the same reader, which is presented in Fig. 8(a), is used, just with the updated transceiver.

Apart from the RF-PCB it consists of a two-channel backend, which handles the analog-to-digital-conversion. Stacked on top is a Xilinx Zynq SoC, which controls the timing of the signal processing chain and programs both the PLL chip and the variable gain amplifiers. Communication to the SoC

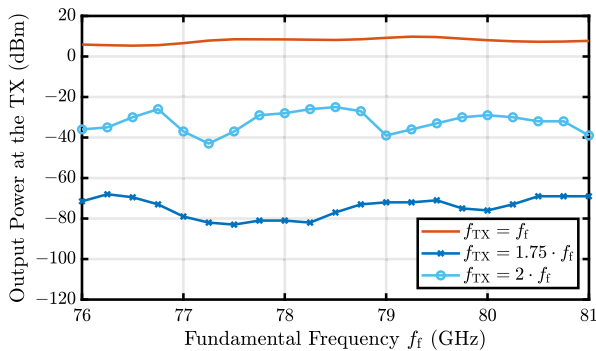


FIGURE 9. Measured output power at the TX. Limited suppression of the frequency expected at the RX, corresponding to $2f_f$ in harmonic radar, results in clutter. The inharmonic radar offers a suppression of up to 91 dB for $1.75f_f$, virtually eliminating the unwanted measurement.

is done via the same USB-interface, that also outputs the resulting measurement data.

B. TAG PCB

The tag PCB is realized on the same layer-stack. Apart from an LDO for the power supply, it only consists of the tag MMIC and the transmit and receive antennas, respectively, which can be seen in Fig. 8(b). Both are realized as differential series-fed patches to offer an antenna pattern typical for automotive applications, with a broad radiation in azimuth and a focus in elevation. The TX antenna for the 134–141 GHz frequency range achieves a maximum simulated gain of 14 dBi, which is slightly above the 12 dBi of fundamental RX antenna. Their respective simulated radiation patterns in azimuth are depicted in Fig. 8(c), respectively.

V. MEASUREMENT RESULTS

With the reader and tag in place, the resulting system can be tested for functionality of the novel approach of utilizing a fractional multiplication factor. Furthermore, the capabilities and limitations regarding clutter rejection, spectral purity and range are investigated in individual measurements.

A. SPECTRAL PURITY OF THE TX

To investigate the system's transmit channel, its output power in the automotive frequency range is firstly measured by itself. Therefore, a PM5B power meter by Virginia Diodes is directly screwed to the TX output of the system, as shown in [21]. The results of the measurement are shown in Fig. 9. It reaches up to 9.8 dBm, matching the expectations of the 15 dBm measured on-chip minus the bond-wire interface and waveguide transition very well.

Furthermore, one potential clutter source known from harmonic radar is investigated. As the increased SCR relies on utilizing separate frequencies for transmitter and receiver, it is degraded if the former also sends out the frequencies expected at the latter. As discussed in [44] and in Section V-C of this article, this leads to parasitic peaks in the receive channel that should ideally be clutter-free. Thus, the output power

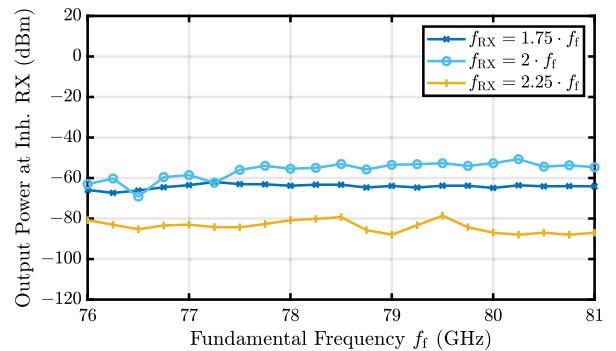


FIGURE 10. Measured output power at the RX. Limited reverse isolation can result in a parasitic measurement of clutter. Most relevantly, the inharmonic at $1.75f_f$ stays below -60 dBm for the whole frequency range.

at those frequencies is determined in a second measurement. Therefore, the system is screwed onto a WR6.5-SAX from Virginia Diodes, which is connected to a UXA from Keysight Technologies.

Unfortunately for harmonic radar, a transmit channel also parasitically generates the 2nd harmonic of the desired output frequency [45]. The TX of this work being no exception. While a suppression such as the shown 40 dB compared to the fundamental is considered sufficient in most other applications, it can lower the SCR in harmonic radar.

In this presented inharmonic radar, however, this path can be considered virtually eliminated. Due to the unique multiplication factor of 1.75, no distinct power is generated by the TX at the inharmonic frequencies. This was verified by measuring the TX of the harmonic radar presented in [21]. At the output of the inharmonic radar, some power was measurable, which is most likely overcoupling from the receive channel, either on-chip or through the bond-wires. Nevertheless, it offers an additional suppression in the range of 30–40 dB. Thus, reaching a maximum suppression of up to 91 dB compared to the desired fundamental.

B. OUTPUT POWER AT THE RX

Similarly to the TX, parasitically sent out signals at the RX can also decrease the SCR. Thus, the output power at the waveguide of the inharmonic RX is also determined with the WR6.5-SAX and UXA. The results of that measurement are presented in Fig. 10.

A maximum value of just under -50 dBm was determined for the harmonic. Thus, being significantly lower and therefore negligible compared to its equivalent at the TX. More relevantly, the inharmonic stays below -60 dBm for the whole frequency range, while the undesired sideband is even lower. Compared to the simulated LO-power of 0 dBm at the mixer input, this represents significant reverse isolation due to the two-stage LNA.

C. CLUTTER REJECTION

As the clutter rejection and corresponding SCR is the key benefit of (in)harmonic radar, it is subsequently investigated

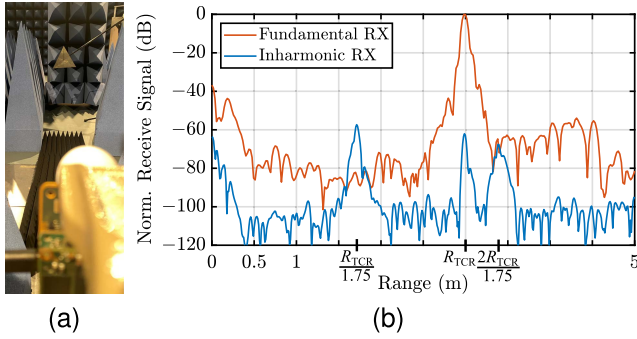


FIGURE 11. Measurement setup in (a) and reflected signal from the reflector for the fundamental and inharmonic RX in (b). The reflector causes clutter at three distances due to paths also known from harmonic radar with a suppression of about 60 dB, respectively.

quantitatively. Therefore, a trihedral corner reflector with an edge length of $\sqrt{2}a = 27$ cm is placed at a distance of 3 m from the reader in an anechoic chamber, as can be seen in Fig. 11(a). Its calculated RCS of 25.6 dBsm at 77 GHz is more than 10 dB higher than a mid-sized car viewed from the rear [46]. To maximize the ratio of the reflected power of the corner compared to the quantization noise, the VGAs of the receivers are programmed to utilize the full input range of the ADC. Thus, this configuration serves as an estimate for a scenario that is as challenging as possible. Nevertheless, since the corner reflector is considered clutter, it should ideally not cause any visible reflections in the inharmonic receiver.

1) PEAK POSITIONS

A range plot for both receivers of the reader for a transmit chirp of 76.57–80.57 GHz corresponding to $B_{TX,f} = 4$ GHz is depicted in Fig. 11(b). That chirp was chosen, as its inharmonic with a factor of 1.75 equals 134–141 GHz. The same, traditional FMCW signal processing can be applied to both receive channels. As the only difference, the inharmonic range R_i is scaled by the tag’s multiplication factor compared to the fundamental range R_f due to the increasing inharmonic bandwidth $B_{RX,i}$ and therefore ramp slope of the expected tag signal, corresponding to

$$R_i = \frac{B_{TX,f} \cdot R_f}{B_{RX,i}} = \frac{B_{TX,f} \cdot R_f}{1.75B_{TX,f}} = \frac{R_f}{1.75}. \quad (5)$$

In the fundamental RX, one very strong peak caused by the corner reflector at the range R_{TCR} can be observed. Instead of being fully clutter-free, the inharmonic RX shows three distinct reflections. Compared to the peak in the fundamental RX, their levels are lower by 57 dB, 62 dB, and 68 dB, respectively. Therefore, offering significant clutter rejection only visible due to the very high Signal-to-noise ratio (SNR) offered by the presented radar. Furthermore, the position of the reflections can be explained with parasitic paths already known from similar phenomena in harmonic radar [44].

Firstly, as [44] has shown, the very high transmitted power at the fundamental can couple back into the IF-signal through the transmitter. After parasitic down-conversion in the mixer,

it introduces a peak closer than the target’s distance. Being based on the parasitic fundamental chirp bandwidth $B_{p,f}$ being half of the expected receive bandwidth, it corresponds to $R_{TCR}/2$ for harmonic radar. Due to the different relation of the range axes’ scaling, the same effect causes the peak to appear at

$$R_{p,1} = \frac{B_{p,f} \cdot R_{TCR}}{B_{RX,i}} = \frac{B_{TX,f} \cdot R_{TCR}}{1.75B_{TX,f}} = \frac{R_{TCR}}{1.75} \quad (6)$$

for the presented inharmonic radar. Due to the modular nature of the utilized chipset, this effect should be preventable in the future, by using a different MMIC for transmission of the fundamental and reception of the inharmonic. For example, by re-designing the reader PCB to utilize the TX of the fundamental transceiver also located on the board.

Secondly, we cover the parasitic reflection at R_{TCR} , likely corresponding to the most plausible location for a peak to appear. In harmonic radar, this is caused by a parasitic transmission of the frequency expected back from the tag from two sources. The first of those being the limited suppression of the harmonic frequency in the transmitter, as discussed in the Section V-A. The concept presented in this article offers the benefit of not transmitting the inharmonic at the TX, previously shown in Fig. 9. However, parasitic transmission through the RX corresponding to the other source still remains. This was therefore discussed in Section V-B with measurements shown in Fig. 10. As the parasitically sent out chirp offers the same bandwidth $B_{p,i}$ as the expected tag signal, it corresponds to

$$R_{p,2} = \frac{B_{p,i} \cdot R_{TCR}}{B_{RX,i}} = \frac{1.75B_{TX,f} \cdot R_{TCR}}{1.75B_{TX,f}} = R_{TCR} \quad (7)$$

after down-conversion. Utilizing a subharmonic receive-mixer for down-conversion could potentially improve the suppression of this parasitic peak due to reducing the power sent out at the inharmonic otherwise known as LO leakage [47].

Third and finally, the peak appearing slightly behind it is the only one somewhat specific to inharmonic radar. It can, however, be explained similarly to the second one, with the previously neglected path. The fairly constant suppression of the harmonic in the range of 40 dB in the TX is theoretically not an issue for inharmonic radar, where it does not correspond to the expected RX frequency. However, the measurement of the inharmonic down-conversion mixer in Fig. 5(b) has shown its ability to also down-convert the harmonic with a suppression of 22–42 dB. Therefore, corresponding to a minimum of 62 dB, fitting the measured 68 dB very well. It should be noted, that the free-space path loss and different conversion gain compared to the fundamental, and the bond-wires not included in the on-chip measurement will shift those values slightly. Since the parasitic harmonic bandwidth $B_{p,h}$ is twice as high, the position of this reflection can be calculated as

$$R_{p,3} = \frac{B_{p,h} \cdot R_{TCR}}{B_{RX,i}} = \frac{2B_{TX,f} \cdot R_{TCR}}{1.75B_{TX,f}} = \frac{2R_{TCR}}{1.75}, \quad (8)$$

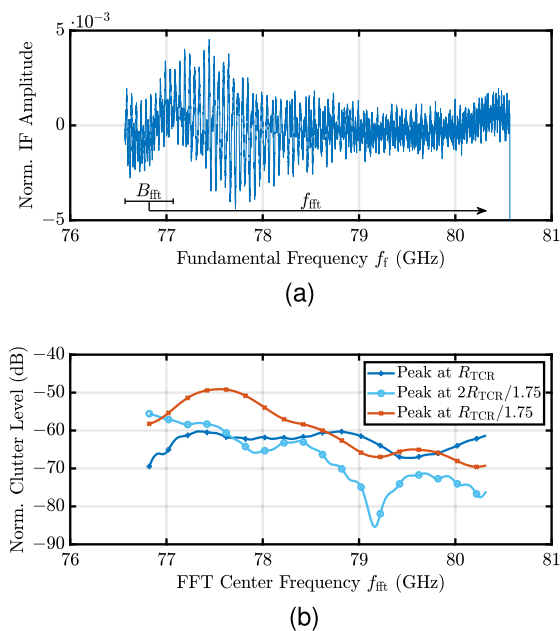


FIGURE 12. IF amplitude of the clutter measurement normalized to the ADCs input range in (a) and the clutter level of the three peaks compared to the fundamental corner reflection for an FFT bandwidth of $B_{\text{fit}} = 500$ MHz in dependency of the FFT center frequency f_{fit} in (b).

fitting the measurement. To further lower this parasitic peak beyond detectability, the level of the harmonic can be given greater consideration in the design process of the TX and RX.

Nevertheless, compared to harmonic radar, where $R_{p,3} = R_{\text{TCR}}$, significant additional suppression can be gained in the receiver. As Fig. 5(b) shows, that suppression varies over input frequency. Thus, the dependency of the levels of the three peaks on the transmitted f_f is subsequently investigated.

2) FREQUENCY DEPENDENCY

Therefore, Fig. 12(a) shows the raw IF data for the inharmonic receiver of the previous clutter rejection measurement in dependency of the fundamental frequency sent out at the TX. Its amplitude is normalized to the maximum input range of the ADC. It is already apparent, that the overall suppression improves for a higher fundamental frequency. Instead of utilizing the full chirp as in Fig. 11(b), a fast-fourier-transform (FFT) for a transmit bandwidth of $B_{\text{fit}} = 500$ MHz is performed to make a more precise statement. Additionally, the FFT center frequency f_{fit} is moved along the chirp. The height of the parasitic peaks in the inharmonic RX are normalized to the desired peak in the fundamental RX to showcase the normalized clutter level in Fig. 12(b).

The coupling through the TX seems to decrease for higher f_{fit} causing the power level of the peak at $R_{\text{TCR}}/1.75$ to go down. While showing some variation, the peak at R_{TCR} has a fairly constant power level, not trending in either direction. Thus corresponding to the output power of the inharmonic at the RX, shown in Fig. 10, and its conversion gain when down-converting, shown in Fig. 5(b), also being fairly constant. Lastly, the peak at $2R_{\text{TCR}}/1.75$ also goes down with

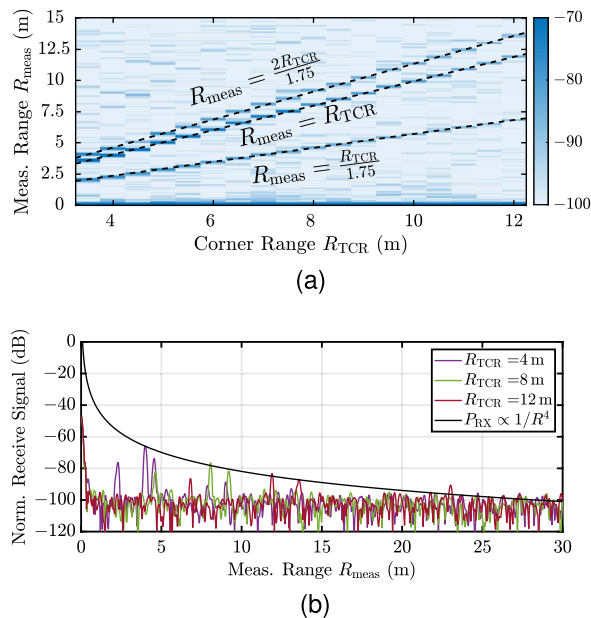


FIGURE 13. Range-plots for an increasing R_{TCR} with the gradient of the target reflections fitting the explained causes in (a) and the plots for an R_{TCR} of 4 m, 8 m, and 12 m, respectively, in (b). The parasitic peaks disappear at just above 20 m due to the $1/R^4$ proportionality.

increasing f_{fit} . The improvement from beginning to end of the chirp corresponds to about 20 dB, thereby matching the enhanced suppression in the down-conversion of Fig. 5(b). The additional dip at slightly over 79 GHz could correspond to an additionally lower output power at the TX, as indicated by Fig. 9.

3) RANGE DEPENDENCY

To conclude the subsection on clutter rejection, the range dependency of the parasitic peaks is subsequently investigated. Therefore, the corner reflector is moved from a distance of 3.5 m to 12 m in 0.5 m steps. The resulting array of range-plots in dependency of the corner distance R_{TCR} and the range of the individual measurement R_{meas} with an intensity representing the received amplitude is presented in Fig. 13(a).

This illustration emphasizes the origin of the parasitic peaks additionally, compared to the individual measurement, as the measured distance moves away with different gradients. With each gradient corresponding to the peak position determined by the individual 3 m measurement. Furthermore, the range dependency of the amplitude is visualized through the individual measurements at 4 m, 8 m, and 12 m, shown in Fig. 13(b).

As the parasitic peaks are caused by fundamental radar measurements at different frequencies, the received amplitude is expected to decrease with $1/R^4$. This behavior is proven by the measurement, whereby the peaks should disappear into the noise floor at just above 20 m. Most significantly, this deviates from the behavior expected from the tag, which should offer a $1/R^2$ -proportionality as explained in Section II. Therefore, the SCR of the tag should improve with range.

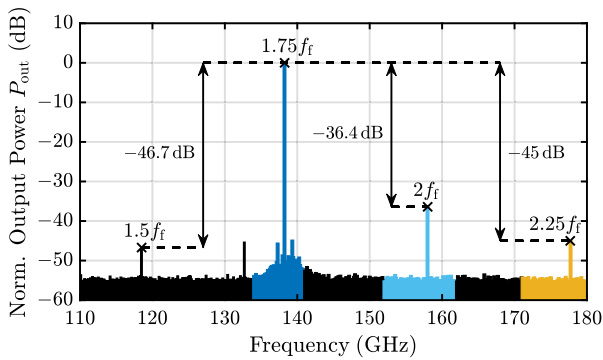


FIGURE 14. Output spectrum of the tag measured in free-space. The signal of $1.75f_f$ is clearly the strongest. Compared to the on-chip results of [25] the suppression of other components is additionally improved due to the differential output, bond-wire focused output matching, and filtering by the antenna.

In summary, three parasitic peaks in the inharmonic receiver for a large corner reflector were observed. The origin of all three parasitic peaks could be determined, explaining the respective positions. Additionally, the knowledge of the causes can be used to improve the already high suppression in the range of 60 dB further, with specific measures given for each path.

D. SPECTRAL PURITY OF THE TAG RESPONSE

After measuring the spectral purity of the tag MMIC single-endedly on-chip in [25], the effect of the differential output and filtering of the antennas can be determined in free-space with the tag PCB. Therefore, its output signal is measured by attaching an antenna to the WR6.5-SAX and aligning it with the TX antenna of the tag. For providing the input signal at the fundamental, the LO module presented in [48] based on the chip of [49] was chosen. As that frequency synthesizer generates the required frequency fundamentally, with very low harmonics and no inharmonics, the measured suppression of the overtones is not limited by those of the TX signal. Instead, ensuring the measured spectrum stemming solely from the tag.

This very spectrum, measured with an $f_f = 79$ GHz, is presented in Fig. 14. The desired output frequency of $1.75f_f = 138.25$ GHz clearly exhibits the highest output level. As in the on-chip measurements, the feed-through of the frequency doubler and the upper sideband of the SSB-mixer conversion of (1) are also observable. However, with a normalized P_{out} of -36.4 dB and -45 dB, respectively, they are suppressed significantly. Compared to the on-chip results of [25], this corresponds to additional improvements of 14.6 dB and 21.2 dB, respectively, thanks to the differential output, bondwire-matching and antenna filtering. Combined with the reduced ability to receive those frequencies shown in Fig. 5(b), the amplitude of the IF-signal caused by those spectral components at that f_f should be attenuated by 71.4 dB and 105 dB, respectively. Therefore, the other components caused by the more complex frequency conversion approach of the

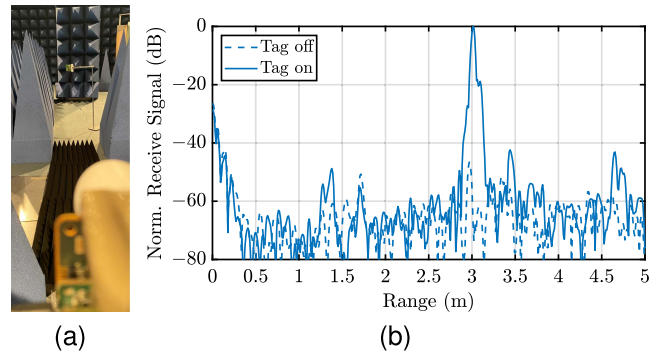


FIGURE 15. Measurement setup in (a) and the measured response in the inharmonic receiver with the tag turned on and off in (b). It is detectable with an SNR of about 60 dB and shows a very low amount of disturbances, even compared to doubling tags.

proposed inharmonic radar should have little to no effect on the tag detection.

E. TAG DETECTION

After investigating the system's rejection of non-tagged object and the tag-response by itself, respectively, the detectability of the tag in conjunction with the reader is subsequently investigated. Therefore, instead of the corner reflector, the tag is placed at the 3 m distance from the reader in the anechoic chamber, as depicted in Fig. 15(a).

Subsequently, the response at the inharmonic receiver with the tag turned off and on is measured and presented in Fig. 15(b). With the tag turned off, only very low levels of the parasitic peaks discussed in detail in Section V-C are visible. With the tag turned on, mainly one strong peak at the position of the tag R_{tag} appears with an SNR of about 60 dB. Apart from that, some increases at specific distances can be observed, including $2R_{tag}/1.75$, slightly farther than $1.5R_{tag}$ and slightly closer than $R_{tag}/2$. However, even compared to active harmonic tags based on just frequency doubling, such as [19], those disturbances are similarly low, with no discernible disadvantage due to the inharmonic concept.

F. MAXIMUM RANGE INVESTIGATION

As the maximum detectable range is an important aspect for most applications, including automotive, it is subsequently investigated inside a long hallway. Therefore, the distance to the tag is increased from 4 m with a step size of 1 m until no response is recorded. The results of that measurement are presented in Fig. 16.

Up to a distance of slightly above 20 m, the power received from the tag only decreases with $1/R^2$ due to it being in saturation. For higher ranges, it starts to decrease proportionally to $1/R^6$ up to a distance of 28 m. Afterward, the tag cannot be detected anymore. Thus, following the analytical considerations made in (4) of Section II. The maximum detection range therefore lies within the capabilities of short-range automotive radar systems. Given that most accidents with vulnerable road

TABLE 1 State-of-the-Art (In)harmonic Radar Sensors With High Relevance to This Work

Ref.	Year	Waveform	Freq. (GHz)	N	BW* (GHz)	P_{TX} (dBm)	$G_{TX,f}$ (dBi)	$G_{RX,h/i}$ (dBi)	$G_{TX,h/i}$ (dBi)	$G_{RX,f}$ (dBi)	Range (m)	$P_{DC,tag}$ (mW)	Spectral Compliance
This	2024	FMCW	80 / 80 & 140	1.75	1.75 / 7	9	28	33	14	12	28	396	Yes
[21]	2022	FMCW	80 / 80 & 160	2	4	9	28	34	12	12	80	89.1	No
[11]	2022	FMCW	14 / 28	2	1	23	25	18	15	17	46	0	No
[19]	2020	FMCW	61 / 122	2	8	6	21	22.2	7.5	7.1	23	132	Yes†
[50]	2020	FMCW	2.9 / 5.8	2	0.16	34.7	13	14	#	#	40	0	No
[50]	2020	FMCW	9.3 / 18.6	2	0.16	40	15	15	#	#	15	0	No
[7]	2008	FMCW	5.95 / 11.9	2	0.2	20	22	22	5.5	2.8	58	0	No
[51]	2016	PRN	9.4 / 18.8	2	0.025	32.4	38	43	0.2	0.2	180	0	No
[52]	2019	Pulsed	9.4 / 18.8	2	-	60	26.5	27.3	#	#	470	0	No
[9]	2021	SFCW	2.9 / 5.8	2	0.1 0.05	50	27	27	2 5	3 3	1020 5800	0 6.6	Yes†
[15]	2021	CW	24 / 72	3	-	30	15	8.3	8.3	15	1	0	No

*Refers to the (in)harmonic BW. The new band offers up to 7GHz. Measurements used a 1 GHz transmit chirp, typical for automotive.

#No gain is given in the publication.

†Not regulated for automotive applications.

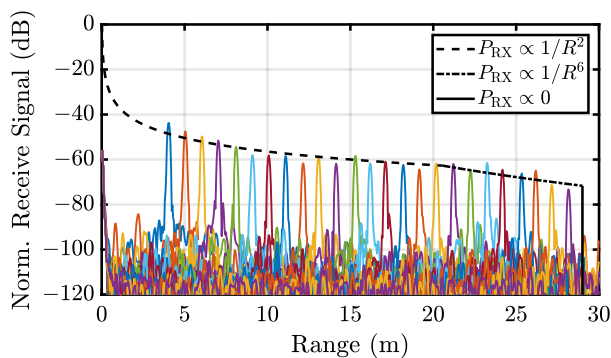


FIGURE 16. The tag response for increasing distance to the reader with a step-size of 1 m. A maximum detectable range of 28 m is achieved, with the received amplitude following the analytical proportionalities with some variance due to alignment.

users, that could be equipped with the tag, occur in inner cities, this corresponds to an adequate range, that can be improved further in the future.

VI. COMPARISON TO THE STATE OF THE ART

To position the novel inharmonic radar concept in the state of the art, it is compared to different existing harmonic radar systems in Table 1. The fairest comparison is of course with our own harmonic radar system based on the same TX output power, reader PCB, and antennas. This shows that the achievable distance has been reduced from 80 m to 28 m, despite the higher power consumption of the tag. As the previous measurement results regarding clutter rejection and spectral purity of tag detection did not show any notable disadvantages, this is viewed as the concept's biggest drawback.

Regarding the increased power consumption, additional components are necessary for the novel frequency conversion. When it comes to the decreased range, the conversion gain of the inharmonic tag is slightly lower, with saturation reached

about 4 dB later in the on-chip measurement [25]. In the configuration utilized in the system measurements, the difference is slightly higher, reducing the saturation range from 47 m to just above 20 m. It should be noted, that an additional gain of 12 dB at the tag's input would quadruple the range to above 80 m, with stability constraints applying. Additionally, the utilization of the divider results in a shorter range of the $1/R^6$ region due to the tag turning off. This could be extended in the future, by increasing the divider sensitivity.

The concept's biggest benefit, however, is its spectral compliance. As Table 1 proves, this is something harmonic radar systems typically struggle with, as they need two frequency bands for the same application separated by an integer ratio. In the case of [19] this is the case for a varying harmonic bandwidth for ISM applications depending on the country. The approach of [9] combines the S-band maritime mobile navigation radar band at 2.9 GHz with 5.8 GHz within the ISM and SRD frequency allocation for maritime search and rescue, with a claim to be spectrally compliant. However, the same cannot be stated when using the identical TX frequency for insect tracking, as done in [53]. It and the other systems mostly focus on utilization in research while neglecting the implications of using the respective frequencies.

This work has proven the validity of fractional multipliers inside a system, therefore relaxing the requirements of the relation between the two bands. In our case, the novel inharmonic radar enables the combination of the current automotive band at 76–81 GHz with the future band at 134–141 GHz for vulnerable road user detection, which was not possible by frequency doubling.

VII. CONCLUSION

In this article, we presented an inharmonic radar system, which, to the best of the authors' knowledge, is the first of its kind. Compared to harmonic radar, where frequency multiplication by an integer, traditionally doubling, is used, we successfully implemented a fractional ratio. The realized

system is capable of conducting conventional radar measurements and detecting an inharmonic tag simultaneously, in two receive channels. Thus allowing for regular automotive radar measurements at 76–81 GHz, while detecting vulnerable road users with their lower RCS in a separate, nearly clutter-free receive channel at 134–141 GHz.

Therefore, we presented an inharmonic transceiver with one TX at the fundamental and two RX at the inharmonic. Together with the tag presented in [25] and assembled onto the PCB of [21], it successfully makes up the inharmonic radar system. Its clutter rejection was subsequently investigated in detail, achieving a suppression of three peaks created by one target of 60 dB. The cause of each peak was explainable by paths also present in harmonic radar, with one specifically benefiting from the inharmonic approach. For the inharmonic tag, an SNR of 60 dB at a distance of 3 m was achieved, with the additional spectral components of the fractional frequency multiplication having no discernible negative impact on spectral purity. It was observable up to a range of 28 m, while still offering sufficient SNR.

The only discernible disadvantage, compared to state-of-the-art harmonic radar systems, was the decreased range per power consumption of the tag. This is due to the current drawn by the additional components of the fractional multiplication and the divider's input sensitivity. What remains, however, is the big advantage of addressing the necessity for harmonic radar, to have two frequency bands available that are exactly separated by an integer value. For automotive radar specifically, the presented inharmonic radar is instead able to introduce spectral compliance for the tag-based detection via the fractional frequency multiplication.

ACKNOWLEDGMENT

The authors would like to thank Infineon Technologies AG for fabricating the chips. Additionally, they would like to thank Steffen Hansen for his input regarding the stability constraints and Annika Braun for her support in conducting the system measurements.

REFERENCES

- [1] J. Shefer and R. J. Klensch, "Harmonic radar helps autos avoid collisions," *IEEE Spectr.*, vol. 10, no. 5, pp. 38–45, May 1973, doi: [10.1109/MSPEC.1973.5217022](https://doi.org/10.1109/MSPEC.1973.5217022).
- [2] A. Merlo, "Automotive radar for the prevention of collisions," *IEEE Trans. Ind. Electron. Control Instrum.*, vol. IECl- 11, no. 1, pp. 1–6, Feb. 1964, doi: [10.1109/TIECI.1964.234462](https://doi.org/10.1109/TIECI.1964.234462).
- [3] J. Hasch, E. Topak, R. Schnabel, T. Zwick, R. Weigel, and C. Waldschmidt, "Millimeter-wave technology for automotive radar sensors in the 77GHz frequency band," *IEEE Trans. Microw. Theory Techn.*, vol. 60, pp. 845–860, Mar. 2012, doi: [10.1109/TMTT.2011.2178427](https://doi.org/10.1109/TMTT.2011.2178427).
- [4] S. Alland, W. Stark, M. Ali, and M. Hegde, "Interference in automotive radar systems: Characteristics, mitigation techniques, and current and future research," *IEEE Signal Process. Mag.*, vol. 36, no. 5, pp. 45–59, Sep. 2019, doi: [10.1109/MSP.2019.2908214](https://doi.org/10.1109/MSP.2019.2908214).
- [5] B. Colpitts, D. Luke, G. Boiteau, and M. Doyle, "Harmonic radar identification tag for insect tracking," in *Proc. Eng. Solutions Next Millennium IEEE Can. Conf. Elect. Comput. Eng.*, 1999, pp. 602–605, doi: [10.1109/CCECE.1999.807936](https://doi.org/10.1109/CCECE.1999.807936).
- [6] B. G. Colpitts and G. Boiteau, "Harmonic radar transceiver design: Miniature tags for insect tracking," *IEEE Trans. Antennas Propag.*, vol. 52, no. 11, pp. 2825–2832, Nov. 2004, doi: [10.1109/TAP.2004.835166](https://doi.org/10.1109/TAP.2004.835166).
- [7] D. Psychoudakis, W. Moulder, C.-C. Chen, H. Zhu, and J. L. Volakis, "A portable low-power harmonic radar system and conformal tag for insect tracking," *IEEE Antennas Wireless Propag. Lett.*, vol. 7, pp. 444–447, 2008, doi: [10.1109/LAWP.2008.2004512](https://doi.org/10.1109/LAWP.2008.2004512).
- [8] K. Grasegger, G. Strapazzon, E. Procter, H. Brugger, and I. Soteras, "Avalanche survival after rescue with the RECCO rescue system: A case report," *Wilderness Environ. Med.*, vol. 27, pp. 282–286, Jun. 2016, doi: [10.1016/j.wem.2016.02.004](https://doi.org/10.1016/j.wem.2016.02.004).
- [9] T. Harzheim, M. Mühlmeier, and H. Heuermann, "A SFCW harmonic radar system for maritime search and rescue using passive and active tags," *Int. J. Microw. Wireless Technol.*, vol. 13, no. 7, pp. 691–707, 2021, doi: [10.1017/s1759078721000520](https://doi.org/10.1017/s1759078721000520).
- [10] A. Orth et al., "A compact harmonic radar system at 61/122 GHz ISM band for physiological joint angle estimation," in *Proc. 19th Eur. Radar Conf.*, 2022, pp. 185–188, doi: [10.23919/EuRAD54643.2022.9924907](https://doi.org/10.23919/EuRAD54643.2022.9924907).
- [11] C. Lynch, A. O. Adeyeye, A. Eid, J. G. D. Hester, and M. M. Tentzeris, "5G/mm-Wave fully-passive dual rotman lens-based harmonic mmID for long range microlocalization over wide angular ranges," *IEEE Trans. Microw. Theory Techn.*, vol. 71, no. 1, pp. 330–338, Jan. 2023, doi: [10.1109/TMTT.2022.3227925](https://doi.org/10.1109/TMTT.2022.3227925).
- [12] S. Hansen, S. Nowok, A. Shoykhetbrod, S. Wickmann, J. Wessel, and N. Pohl, "Distributed sensor network for 3D tag localization using harmonic radar at 61/122 GHz ISM band," in *Proc. 20th Eur. Radar Conf.*, 2023, pp. 343–346, doi: [10.23919/EuRAD58043.2023.10289328](https://doi.org/10.23919/EuRAD58043.2023.10289328).
- [13] G. A. Vera, Y. Duroc, and S. Tedjini, "Third harmonic exploitation in passive UHF RFID," *IEEE Trans. Microw. Theory Techn.*, vol. 63, no. 1, pp. 2991–3004, Sep. 2015, doi: [10.1109/TMTT.2015.2455495](https://doi.org/10.1109/TMTT.2015.2455495).
- [14] D. Kumar, S. Mondal, S. Karuppuswami, Y. Deng, and P. Chahal, "Harmonic RFID communication using conventional UHF system," *IEEE J. Radio Freq. Identif.*, vol. 3, no. 4, pp. 227–235, Dec. 2019, doi: [10.1109/JRFID.2019.2925527](https://doi.org/10.1109/JRFID.2019.2925527).
- [15] A. Mishra and C. Li, "A third-order harmonic radar design for mm-wave frequencies," *Radar Sensor Technol.* XXV, vol. 11742, 2021, Art. no. 117421, doi: [10.1117/12.2586111](https://doi.org/10.1117/12.2586111).
- [16] V. Palazzi et al., "Low-power frequency doubler in cellulose-based materials for harmonic RFID applications," *IEEE Microw. Wireless Compon. Lett.*, vol. 24, no. 12, pp. 896–898, Dec. 2014, doi: [10.1109/LMWC.2014.2361431](https://doi.org/10.1109/LMWC.2014.2361431).
- [17] S. Mondal and P. Chahal, "A passive harmonic RFID tag and interrogator development," *IEEE J. Radio Freq. Identif.*, vol. 3, no. 2, pp. 98–107, Jun. 2019, doi: [10.1109/JRFID.2019.2910234](https://doi.org/10.1109/JRFID.2019.2910234).
- [18] T. Jaeschke, C. Bredendiek, S. Küppers, and N. Pohl, "High-precision D-band FMCW-Radar sensor based on a wideband SiGe-Transceiver MMIC," *IEEE Trans. Microw. Theory Techn.*, vol. 62, no. 12, pp. 3582–3597, Dec. 2014, doi: [10.1109/TMTT.2014.2365460](https://doi.org/10.1109/TMTT.2014.2365460).
- [19] S. Hansen, C. Bredendiek, G. Briese, and N. Pohl, "A compact harmonic radar system with active tags at 61/122 GHz ISM band in SiGe BiCMOS for precise localization," *IEEE Trans. Microw. Theory Techn.*, vol. 69, no. 1, pp. 906–915, Jan. 2021, doi: [10.1109/TMTT.2020.3026353](https://doi.org/10.1109/TMTT.2020.3026353).
- [20] T. T. Braun, J. Schöpfel, C. Schweer, and N. Pohl, "A harmonic automotive radar for bicycle detection with RFID tags at 79/158 GHz," in *Proc. IEEE MTT-S Int. Microw. Symp.*, 2022, pp. 526–529, doi: [10.1109/IMS37962.2022.9865601](https://doi.org/10.1109/IMS37962.2022.9865601).
- [21] T. T. Braun, J. Schöpfel, P. Kwiatkowski, C. Schweer, K. Aufinger, and N. Pohl, "Expanding the capabilities of automotive radar for bicycle detection with harmonic RFID tags at 79/158GHz," *IEEE Trans. Microw. Theory Techn.*, vol. 71, no. 1, pp. 320–329, Jan. 2023, doi: [10.1109/TMTT.2022.3219541](https://doi.org/10.1109/TMTT.2022.3219541).
- [22] T. T. Braun, J. Schöpfel, and N. Pohl, "Detecting vulnerable road users utilizing the harmonic RCS of active tags at 79/158 GHz," in *Proc. IEEE Radar Conf.*, 2023, pp. 1–5, doi: [10.1109/RadarConf2351548.2023.10149776](https://doi.org/10.1109/RadarConf2351548.2023.10149776).
- [23] "Radio frequency channel/block arrangements for fixed service systems operating in the bands 130–134 GHz 141–148.5 GHz 151.5–164 GHz and 167–174.8 GHz," *Electron. Commun. Committee*, Apr. 2018. [Online]. Available: <https://docdb.cept.org/document/2012>
- [24] M. J. Marcus, "6G spectrum policy issues above 100GHz," *IEEE Wireless Commun.*, vol. 28, no. 6, pp. 7–8, Dec. 2021, doi: [10.1109/MWC.2021.9690484](https://doi.org/10.1109/MWC.2021.9690484).

- [25] T. T. Braun, J. Schöpfel, C. Bredendiek, and N. Pohl, "Connecting the automotive bands of present and future with a tag for inharmic radar at 76–81/134–141GHz," *IEEE Microw. Wireless Technol. Lett.*, vol. 34, no. 4, pp. 451–454, Apr. 2024, doi: [10.1109/LMWT.2024.3362385](https://doi.org/10.1109/LMWT.2024.3362385).
- [26] A. Filippi, V. Martinez, and M. Vlot, "Spectrum for automotive radar in the 140 GHz band in Europe," in *Proc. 19th Eur. Radar Conf.*, 2022, pp. 253–256, doi: [10.23919/EuRAD54643.2022.9924643](https://doi.org/10.23919/EuRAD54643.2022.9924643).
- [27] B. Sene, D. Reiter, H. Knapp, H. Li, T. Braun, and N. Pohl, "An automotive D-band FMCW radar sensor based on a SiGe-transceiver MMIC," *IEEE Microw. Wireless Compon. Lett.*, vol. 32, no. 3, pp. 194–197, Mar. 2022, doi: [10.1109/LMWC.2021.3121656](https://doi.org/10.1109/LMWC.2021.3121656).
- [28] I. Kraus, H. Knapp, D. Reiter, and N. Pohl, "A monostatic D-band Doppler MMIC with very compact i/q mixer realization in SiGe BiCMOS technology," *IEEE Trans. Microw. Theory Techn.*, vol. 72, no. 1, pp. 606–617, Jan. 2024, doi: [10.1109/TMTT.2023.3327864](https://doi.org/10.1109/TMTT.2023.3327864).
- [29] "ECC/DEC/(22)03: Technical characteristics, exemption from individual licensing and free circulation and use of specific radiodetermination applications in the frequency range 116–260GHz," Mar. 2024. [Online]. Available: <https://docdb.cept.org/document/28577>
- [30] A. P. Klapuri, "Multiple fundamental frequency estimation based on harmonicity and spectral smoothness," *IEEE Speech Audio Process.*, vol. 11, no. 6, pp. 804–816, Nov. 2003, doi: [10.1109/TSA.2003.815516](https://doi.org/10.1109/TSA.2003.815516).
- [31] G. J. Mazza, A. F. Martone, K. I. Ranney, and R. M. Narayanan, "Nonlinear radar for finding RF electronics: System design and recent advancements," *IEEE Trans. Microw. Theory Techn.*, vol. 65, no. 5, pp. 1716–1726, May 2017, doi: [10.1109/TMTT.2016.2640953](https://doi.org/10.1109/TMTT.2016.2640953).
- [32] G. Hasenaecker, M. v. Delden, T. Jaeschke, N. Pohl, K. Aufinger, and T. Musch, "A SiGe fractional- N frequency synthesizer for mm-wave wideband FMCW radar transceivers," *IEEE Trans. Microw. Theory Techn.*, vol. 64, no. 3, pp. 847–858, Mar. 2016, doi: [10.1109/TMTT.2016.2520469](https://doi.org/10.1109/TMTT.2016.2520469).
- [33] A. Li, S. Zheng, J. Yin, X. Luo, and H. C. Luong, "A 21–48GHz subharmonic injection-locked fractional- n frequency synthesizer for multiband point-to-point backhaul communications," *IEEE J. Solid-State Circuits*, vol. 49, no. 8, pp. 1785–1799, Aug. 2014, doi: [10.1109/JSSC.2014.2320952](https://doi.org/10.1109/JSSC.2014.2320952).
- [34] S. Shin, D. R. Utomo, H. Jung, S.-K. Han, J. Kim, and S.-G. Lee, "Wide locking-range frequency multiplier by 1.5 employing quadrature injection-locked frequency tripler with embedded notch filtering," *IEEE Trans. Microw. Theory Techn.*, vol. 67, no. 12, pp. 4791–4802, Dec. 2019, doi: [10.1109/TMTT.2019.2937480](https://doi.org/10.1109/TMTT.2019.2937480).
- [35] F. Mustafa, E. Halpern, and E. Socher, "An on-chip active frequency multiplier-by-seven (x -band to w -band) for millimeter-wave signal generation," in *Proc. IEEE Int. Conf. Microw. Commun. Antennas Electron. Syst.*, 2015, pp. 1–3, doi: [10.1109/COMCAS.2015.7360432](https://doi.org/10.1109/COMCAS.2015.7360432).
- [36] Z. Chen, C.-C. Wang, and P. Heydari, "W-band frequency synthesis using a Ka-band PLL and two different frequency triplers," in *Proc. IEEE Radio Freq. Integr. Circuits Symp.*, 2011, pp. 1–4, doi: [10.1109/RFIC.2011.5940607](https://doi.org/10.1109/RFIC.2011.5940607).
- [37] S. Park et al., "A D-band low-power and high-efficiency frequency Multiply-by-9 FMCW radar transmitter in 28-nm CMOS," *IEEE J. Solid-State Circuits*, vol. 57, no. 7, pp. 2114–2129, Jul. 2022, doi: [10.1109/JSSC.2022.3157643](https://doi.org/10.1109/JSSC.2022.3157643).
- [38] J. Romstadt et al., "A 117.5–155-GHz SiGe $\times 12$ frequency multiplier chain with push-push doublers and a Gilbert cell-based tripler," *IEEE J. Solid-State Circuits*, vol. 58, no. 9, pp. 2430–2440, 2023, doi: [10.1109/JSSC.2023.3284600](https://doi.org/10.1109/JSSC.2023.3284600).
- [39] J. Zhang, Y. Peng, H. Liu, Y. Wu, C. Zhao, and K. Kang, "A 21.7-to-41.7-GHz injection-locked LO generation with a narrowband low-frequency output for multiband 5G communications," *IEEE Trans. Microw. Theory Techn.*, vol. 68, no. 1, pp. 170–183, Jan. 2020, doi: [10.1109/TMTT.2019.2940024](https://doi.org/10.1109/TMTT.2019.2940024).
- [40] J. Schoepfel, T. T. Braun, S. Kueppers, K. Aufinger, and N. Pohl, "A fully differential hybrid coupler for automotive radar applications," in *Proc. 17th Eur. Microw. Integr. Circuits Conf.*, 2022, pp. 107–110, doi: [10.23919/EuMIC54520.2022.9923546](https://doi.org/10.23919/EuMIC54520.2022.9923546).
- [41] S. Henzler and S. Koeppe, "Design and application of power optimized high-speed CMOS frequency dividers," *IEEE Trans. Very Large Scale Integr. (VLSI) Syst.*, vol. 16, no. 11, pp. 1513–1520, Nov. 2008, doi: [10.1109/TVLSI.2008.2001136](https://doi.org/10.1109/TVLSI.2008.2001136).
- [42] J. Schoepfel, S. Kueppers, K. Aufinger, and N. Pohl, "A SiGe transceiver chipset for automotive radar applications using wideband modulation sequences," *Int. J. Microw. Wireless Technol.*, vol. 11, no. 7, pp. 676–685, 2019, doi: [10.1017/S1759078719000849](https://doi.org/10.1017/S1759078719000849).
- [43] B. Welp, A. Meusling, K. Aufinger, and N. Pohl, "A mixed-mode beamforming radar transmitter MMIC utilizing novel ultrawideband IQ-Generation techniques in SiGe BiCMOS," *IEEE Trans. Microw. Theory Techn.*, vol. 66, no. 6, pp. 2604–2617, Jun. 2018, doi: [10.1109/TMTT.2018.2804912](https://doi.org/10.1109/TMTT.2018.2804912).
- [44] S. Hansen and N. Pohl, "Experimental evaluation of filtering and isolation in highly integrated mmWave harmonic radar," in *Proc. 51st Eur. Microw. Conf.*, 2022, pp. 717–720, doi: [10.23919/EuMC50147.2022.9784164](https://doi.org/10.23919/EuMC50147.2022.9784164).
- [45] D. Milanese, S. Bottigliero, M. Saccani, R. Maggiora, A. Viscardi, and M. M. Galesi, "An harmonic radar prototype for insect tracking in harsh environments," in *Proc. IEEE Int. Radar Conf.*, 2020, pp. 648–653, doi: [10.1109/RADAR42522.2020.9114540](https://doi.org/10.1109/RADAR42522.2020.9114540).
- [46] S. B. J. Gowdu, A. Schwind, R. Stephan, and M. A. Hein, "Monostatic RCS measurements of representative road traffic objects in the 76 ... 81 GHz frequency band," in *Proc. IEEE Radar Conf.*, 2020, pp. 1–6, doi: [10.1109/RadarConf2043947.2020.9266391](https://doi.org/10.1109/RadarConf2043947.2020.9266391).
- [47] J.-H. Tsai and T.-W. Huang, "35–65-GHz CMOS broadband modulator and demodulator with sub-harmonic pumping for MMW Wireless gigabit applications," *IEEE Trans. Microw. Theory Techn.*, vol. 55, no. 10, pp. 2075–2085, Oct. 2007, doi: [10.1109/TMTT.2007.905497](https://doi.org/10.1109/TMTT.2007.905497).
- [48] T. T. Braun et al., "A phase-locked loop with a jitter of 50 fs for astronomy applications," *Int. J. Microw. Wireless Technol.*, vol. 15, no. 6, pp. 1012–1020, 2023, doi: [10.1017/s1759078722001386](https://doi.org/10.1017/s1759078722001386).
- [49] T. T. Braun, M. v. Delden, C. Bredendiek, J. Schoepfel, and N. Pohl, "A low phase noise phase-locked loop with short settling times for automotive radar," in *Proc. 16th Eur. Microw. Integr. Circuits Conf.*, 2022, pp. 205–208, doi: [10.23919/EuMIC50153.2022.9783662](https://doi.org/10.23919/EuMIC50153.2022.9783662).
- [50] G. Storz and A. Lavrenko, "Compact low-cost FMCW harmonic radar for short range insect tracking," in *Proc. IEEE Int. Radar Conf.*, 2020, pp. 642–647, doi: [10.1109/RADAR42522.2020.9114612](https://doi.org/10.1109/RADAR42522.2020.9114612).
- [51] Y.-T. Liu, M.-L. Hsu, H. Wang, and Z.-M. Tsai, "A differential miniature transponder for 9.4/18.8 GHz harmonic bee searching radar with low gain degradation from bee's body," in *Proc. IEEE MTT-S Int. Microw. Symp.*, 2016, pp. 1–4, doi: [10.1109/MWSYM.2016.7540016](https://doi.org/10.1109/MWSYM.2016.7540016).
- [52] R. Maggiora, M. Saccani, D. Milanese, and M. Porporato, "An innovative harmonic radar to track flying insects: The case of vespa velutina," *Sci. Rep.*, vol. 9, Aug. 2019, Art. no. 11964, doi: [10.1038/s41598-019-48511-8](https://doi.org/10.1038/s41598-019-48511-8).
- [53] A. Lavrenko, "Effects of bistatic operation in harmonic radar," in *Proc. 19th Eur. Radar Conf.*, 2022, pp. 1–4, doi: [10.23919/eu-rad54643.2022.9924804](https://doi.org/10.23919/eu-rad54643.2022.9924804).



TOBIAS T. BRAUN (Graduate Student Member, IEEE) was born in Duesseldorf, Germany, in 1996. He received the B.Sc. and M.Sc. degrees in electrical engineering and information technology from TU Dortmund, Dortmund, Germany, in 2016 and 2019, respectively. Since 2019, he has been working toward the Ph.D. degree with the Institute of Integrated Systems, Ruhr University Bochum, Bochum. Since 2019, he has been a Research Assistant with the Institute of Integrated Systems, Ruhr University Bochum. His current research

interests include integrated circuit and system design for automotive applications. Tobias T. Braun was the recipient of the EuMIC Young Engineer Prize from European Microwave Week in 2021.



JAN SCHÖPFEL (Member, IEEE) received the B.Sc., M.Sc., and Dr.-Ing. degrees in electrical engineering and information technology from Ruhr University Bochum, Bochum, Germany, in 2014, 2016, and 2024, respectively. Since 2017, he has been with the Institute for Integrated Systems, Ruhr University Bochum. His current research interests include the concepts and integrated circuits for radar sensors for fully autonomous driving. He was the co-recipient of the EuMIC 2021 Best Student Paper Award.



CHRISTIAN BREDENDIEK (Member, IEEE) was born in Gelsenkirchen, Germany, in 1981. He received the Dipl.Ing. and Dr. Ing. degrees in electrical engineering from Ruhr University Bochum, Bochum, Germany, in 2008 and 2014, respectively. From 2008 to 2014, he was a Research Assistant with the Institute of Integrated Systems, Ruhr University Bochum. Since 2015, he has been with the Department of Integrated Circuits and Sensor Systems, Fraunhofer Institute for High Frequency Physics and Radar Techniques FHR, Wachtberg,

Germany. His current research interests include frequency synthesis, working on system concepts and integrated circuits for various mm-Wave applications. Dr. Bredendiek was the recipient of the EuMIC Best Paper Award from European Microwave Week in 2012 and the co-recipient of the EuMIC 2021 Best Student Paper Award.



JUAN JOSE FORERO B. received the bachelor's degrees in electrical engineering and information technology from Ruhr University Bochum, Bochum, Germany, and the Universidad Nacional de Colombia, Bogotá, Colombia, in 2024, as a part of the double degree program between both the universities. He will continue his M.Sc. degree in electrical engineering and information technology with Ruhr University Bochum. Since 2022, he has been with the Institute of Integrated Systems, Ruhr University Bochum, as a working student with a

focus on printed circuit board design for radar systems and operational amplifier circuits.



NILS POHL (Senior Member, IEEE) received the Dipl.-Ing. and Dr.-Ing. degrees in electrical engineering from Ruhr University Bochum, Bochum, Germany, in 2005 and 2010, respectively. From 2006 to 2011, he was a Research Assistant and subsequently from 2011 an Assistant Professor with Ruhr University Bochum. In 2013, he became the Head of the Department of mm-wave radar and high frequency sensors with the Fraunhofer FHR, Wachtberg, Germany. In 2016, he became a Full Professor of Integrated Systems with Ruhr University Bochum.

He has authored or coauthored more than 250 scientific papers and has issued several patents. His current research interests include ultra-wideband mm-wave radar, design, and optimization of mm-wave integrated SiGe circuits and system concepts with frequencies up to 500 GHz and above, frequency synthesis, and antennas. Dr. Pohl is a member of VDE, ITG, EUMA, and URSI. He was the recipient of the IEEE MTT Outstanding Young Engineer Award in 2018, the Best Demo Award at RWW 2015, Best Student Paper Awards at RadarConf 2020, RWW 2021, and EuMIC 2021, and Best Paper Awards at EuMIC 2012, and of the AWPL in 2022.